High-Aspect-Ratio $LiNbO_3$ Ridge Waveguide With Vertical Buffer Layer and Enhanced Electro-Optical Efficiency

Alexis Caspar, Matthieu Roussey, Markus Häyrinen, Janne Laukkanen, Anthony Pérignon, Florent Behague, Venancio Calero, Gwenn Ulliac, Maria-Pilar Bernal, Markku Kuittinen, and Nadège Courjal

***Abstract*—As high aspect ratio ridges are not easy to process with standard lithographic techniques we propose alternative solutions based on atomic layer deposition and precise dicing to allow both uniform coating of the relief surface and a selective lift-off at the top of the ridges. The techniques are successfully employed to demonstrate an electro-optical (EO) low-loss tapered ridge waveguide with 90% of EO overlap coefficient, and a Fabry–Perot-based 150 μm long intensity modulator with a figure of merit 8 times better than a standard Ti-indiffused EO modulator. Furthermore, enhancement is even expected by optimizing the manufacturing of the Fabry–Perot cavity inside the ridge. These developments open the way to active three-dimensional microstructures, not only for optical applications but also for MEMS, acoustic or microfluidic devices.**

***Index Terms*—Atomic layer deposition, electro-optic devices, lithium niobate, precise dicing.**

I. Introduction

PRECISE dicing is a powerful technique for the production of high-aspect-ratio components, with numerous applications in microfluidics [1], spectrometry [2], acoustics [3], and integrated optics [4]. An adequate choice of the blade type and the speed parameters can lead to the wafer-scale production of arrays as deep as 1.5 mm [5], [6], but also to smooth and low-loss guiding ridges and membranes [4], [7]–[9] in various materials [10], [11].

Manuscript received November 14, 2017; revised December 22, 2017; accepted January 26, 2018. Date of publication January 31, 2018; date of current version May 15, 2018. This work was supported in part by the ANR agency under Project CEPAGE (ANR-16-CE24-0024), in part by the SATT Grand-Est program under project "Microguide waveguides," in part by the Labex ACTION program (contract ANR-11-LABX-01-01), and in part by the French RENATECH network and its FEMTO-ST technological facility. *(Corresponding author: Nadège Courjal.)*

A. Caspar, A. Pérignon, F. Behague, V. Calero, G. Ulliac, M.-P. Bernal, and N. Courjal are with the FEMTO-ST Institute, University of Bourgogne Franche-Comté, CNRS, Besançon 25000, France (e-mail: alexis.caspar@femto-st.fr; anthony.perignon@edu.univ-fcomte.fr; florent.behague@femto-st.fr; venancio.calero@femto-st.fr; gwenn.ulliac@femto-st.fr; maria-pilar.bernal@univ-fcomte.fr; Nadege.courjal@femto-st.fr).

M. Roussey, M. Häyrinen, J. Laukkanen, and M. Kuittinen are with the Institute of Photonics, University of Eastern Finland, Joensuu 80101, Finland (e-mail: matthieu.roussey@uef.fi; markus.hayrinen@uef.fi; janne.laukkanen@uef.fi; markku.kuittinen@uef.fi).

Color versions of one or more of the figures in this paper are available online at http://ieeexplore.ieee.org.

Digital Object Identifier 10.1109/JLT.2018.2799995

In particular, $LiNbO_3$ diced ridge waveguides have attracted growing interest over the past decade, because of their ability to confine light in micrometer-square cross sections for the achievement of highly efficient non-linear frequency converters [8], [12], optical amplifiers [13], and ultra-compact and highly-sensitive sensors [14]. The diced ridges can be higher than 100 μm [15] or thinner than 2 μm [7], but heights between 10 μm and 50 μm allow better reproducibility and robustness and are therefore usually preferred. Electro-optic (EO) devices, enabling the control of light, require selective and uniform layers deposited on 10 to 50 μm-high sidewalls, which is a challenging fabrication step. Such a deposition can be carried out by tilting the sample several times during the deposition process [13], but this approach does not yield a precise control of thickness uniformity. On the other hand, Atomic Layer Deposition (ALD) is a well-known technique enabling conformal coatings over high-aspect-ratio structures, and thickness control at the nanometer level [16]. These properties are well appreciated in integrated optics for the production of slot or strip waveguides [17], [18], ring resonators, and many other photonic structures [19]. Here we propose ALD for the uniform coating of a dielectric buffer layer over the high-aspect-ratio ridges. We also show how evaporation can be employed, if a uniform buffer layer is not a critical feature. Finally, we propose an innovative and mask-less lift-off technique to obtain separated electrodes on both sides of the ridge waveguides by selectively dicing the metallic top layer. In comparison with a standard lift-off technique employing chemical removal, this method avoids local tearing and cracks at the electrodes top. Hence, we demonstrate the first compact electro-optical modulator with vertical electrodes separated by a distance of only 6 μm and with low-driving voltage. Two configurations are successively studied: the first one is a tapered-ridge electro-optical waveguide with low insertion losses and an EO efficiency twice better than a standard waveguide. The second one pushes one step further the integration by inscribing a photonic cavity along the optical path for enhanced EO interaction.

II. Description and Model

The ridge-based EO modulator is schematically depicted in Fig. 1. It consists of a high-aspect-ratio Ti-indiffused $LiNbO_3$ tapered-ridge waveguide with vertical electrodes and Fabry-Perot cavity.

0733-8724 © 2018 IEEE. Translations and content mining are permitted for academic research only. Personal use is also permitted, but republication/redistribution requires IEEE permission. See http://www.ieee.org/publications_standards/publications/rights/index.html for more information.

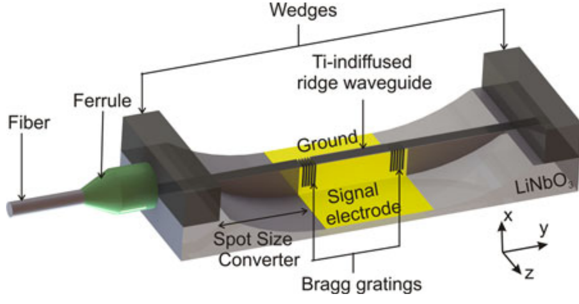

Fig. 1. Schematic diagram of the ridge-based electro-optical component with uniform buffer layer and Spot-Size-Converters to allow easy and low-loss pigtailing. A few hundreds of nanometer thick buffer layer has to be deposited between the electrodes and the waveguide to avoid losses inside the metal.

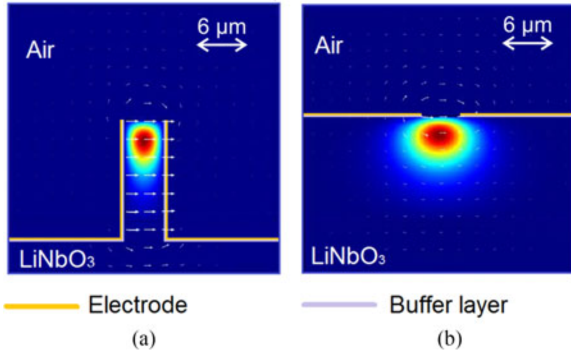

Fig. 2. F.e.m. calculation (comsol software) of the electric fiel (white arrows) and optical TE field. (a) Ridge configuration, $g = 6\,\mu$m, height $=$ 20 μm, thickness of the Al_2O_3 buffer layer $\delta = 200$ nm. (b) Standard Ti-indiffused configuration, with the same separation between electrodes and buffer layer as in (a).

The ridge is made by Ti-indiffusion followed by optical grade dicing. A compromise between lateral confinement and low losses can be found by adjusting the width to 5–7 μm and the height between 10 and 50 μm [15]. Input and output tapers are created by a progressive decrease of the ridge height at the extremities of the ridge waveguide to optimize the mode matching with the fiber [9]. Two vertical electrodes surround the ridge in order to apply a uniformly high electric field on the optical guided-wave. A buffer layer is disposed between the ridge and the electrodes. It prevents from optical leakage inside the metallic electrodes, which would lead to excessive absorption. Finally, the intensity modulator is achieved by inscribing a Fabry-Perot cavity made of two high-aspect-ratio Bragg grating mirrors. The wedges seen in Fig. 1 are bonded at the extremities of the waveguide so as to ease and consolidate the fiber pigtailing.

The EO interaction inside the ridge waveguide is calculated by finite element method (F.E.M.) with COMSOL software. The results are show in Fig. 2(a) for a 6 μm-wide ridge waveguide and they are compared to a standard Ti-indiffused waveguide without ridge in Fig. 2(b). The first advantage of the ridge configuration relies on the uniformity and strength of the applied electric field, which is illustrated by the large and uniform white arrows in Fig. 2(a). Moreover, and contrarily to the standard configuration seen in Fig. 2(b), the applied electric field is totally directed along one axis of the substrate, which makes the internal electric field straightforward to evaluate. In other words, the two vertical electrodes behave as a plan capacitor and the electric field inside the ridge waveguide is simply expressed by (1):

$$E = \frac{\varepsilon_{\text{diel}}}{2 \cdot \varepsilon_{\text{LN}} \cdot \delta + (g - 2 \cdot \delta) \cdot \varepsilon_{\text{diel}}} V \tag{1}$$

where V is the applied voltage, δ is the buffer layer thickness, g is the distance between the two vertical electrodes, and $\varepsilon_{\text{diel}}$, ε_{LN} are the dielectric constants of the buffer layer and lithium niobate, respectively. Here we chose $\delta = 200$ nm to avoid losses into the electrodes and $g = 6\,\mu$m, to achieve both a high optical confinement and low propagation losses; and $\varepsilon_{\text{LN}} = 28$ for an X-cut Y-propagating ridge waveguide. According to (1), the applied electric field is stronger when $\varepsilon_{\text{diel}}$ is close to ε_{LN}. Consequently, we use Al_2O_3 as buffer layer, whose dielectric constant $\varepsilon_{\text{diel}} = 10$ is higher than a traditional silica buffer layer ($\varepsilon_{SiO2} = 3.8$).

The electro-optical overlap coefficient η can be estimated by using (2):

$$\eta = \frac{g}{V} \cdot \frac{\iint \psi^2 \cdot E \cdot \mathrm{d}S}{\iint \psi^2 \cdot \mathrm{d}S} \tag{2}$$

where Ψ denotes the amplitude of the guided optical electric field, and S the cross-section of the waveguide. The uniformity of the internal electric field in the ridge waveguide yields a simpler expression of (2):

$$\eta_{\text{ridge}} = \frac{g \cdot \varepsilon_{\text{diel}}}{2 \cdot \varepsilon_{\text{LN}} \cdot \delta + (g - 2 \cdot \delta) \cdot \varepsilon_{\text{diel}}} \tag{3}$$

Hence, the presented ridge configuration shows a calculated EO efficiency of $\eta_{\text{ridge}} = 90\%$, which is twice higher than in a standard waveguide fabricated in the same conditions and with the same distance $g = 6\,\mu$m between the two coplanar electrodes (see Fig. 2(b)). So the ridge waveguide is expected to reduce two-folds the driving voltage as compared with a standard waveguide.

The challenge is then to deposit vertical buffer layers and electrodes along the vertical walls of the high-aspect-ratio ridge waveguide.

III. Fabrication & Characterization of the Tapered-Ridge EO Waveguide

A. Fabrication

The process flow is schematically depicted in Fig. 3. In a first step (see Fig. 3(a)), 6 μm-wide channel waveguides were fabricated in X-cut $LiNbO_3$ substrates. They were achieved by evaporating the 90 nm thick layer of Ti over the substrate, and by diffusion at 1030 °C for 10 hours. The resulting diffusion depth was $\delta = 4\,\mu$m. Then, an S1813 photoresist was spray-coated over the wafer to the thickness of 5 μm (Fig. 3(b)). In a third step represented in Fig. 3(c), the tapered-ridge waveguides were produced by optical-grade dicing, meaning that the substrate was diced and polished at the same time [9]. The blade was driven to a desired depth d inside the substrate, as schematically depicted in Fig. 3(c). Then, it was translated parallel to the wafer surface with a rotation speed of 10,000 rpm and a moving speed

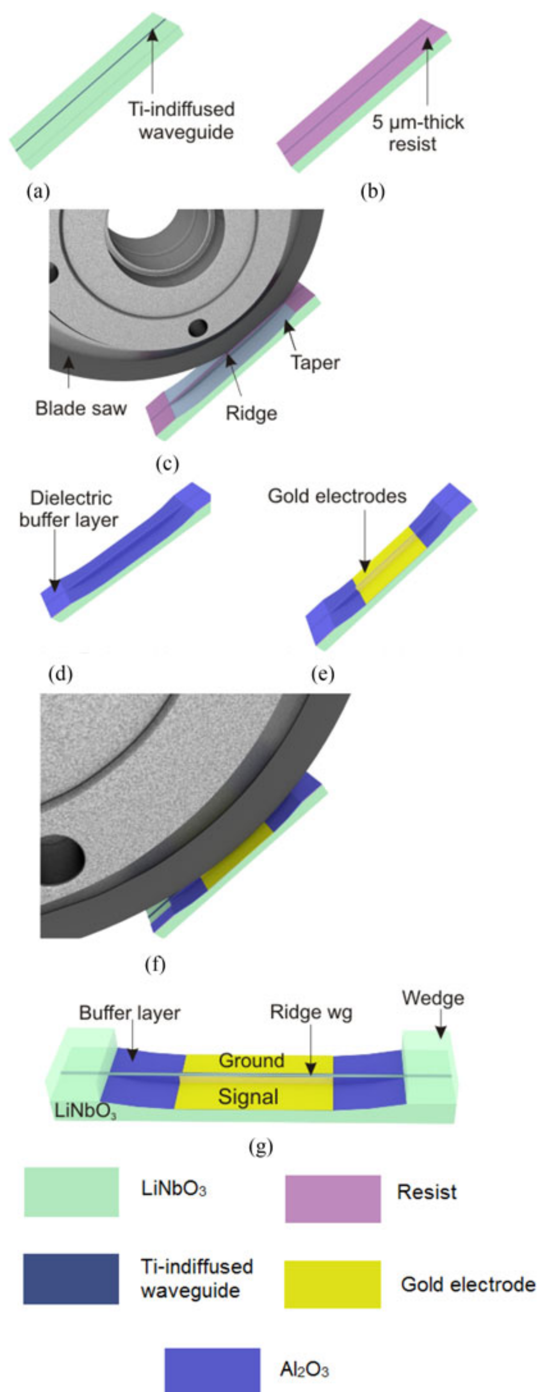

Fig. 3. Fabrication process flow.

of 0.2 mm/s. The ridge waveguides result from the remaining matter between two trenches. The taper was manufactured simultaneously with the ridges by lifting the saw blade before the end of the ridge waveguide. The circular shape of the blade is hence inscribed along the propagation direction of the ridge waveguide, allowing a progressive variation of the ridge height. A distance was left intact between the end of the taper and the output facet, to ease the pigtailing, as represented in Fig. 1. In a fourth step, an O_2 plasma etching was achieved for 10 minutes to favor the adherence of the subsequent depositions. Then,

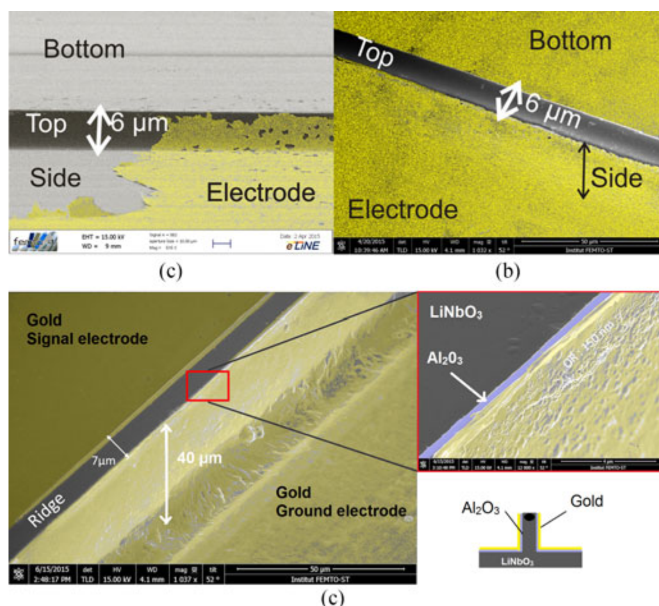

Fig. 4. SEM views of EO ridges made by different techniques. (a) An SiO_2 layer is deposited on the flanks of the ridges in two steps, and the lift-off is done just by using a chemical remover. (b) An SiO_2 layer is deposited on the flanks of the ridges in two steps, and the lift-off is done by precise dicing followed by chemical removing of the resist. (c) Same as in (b), except that the buffer layer is deposited by ALD.

the 200 nm thick layer of Al_2O_3 was deposited over the ridge waveguides by atomic layer deposition (Fig. 3(d)), and this was followed by a sputtering of 40 nm-thick layer of titanium and 160 nm thick layer of gold seen in Fig. 3(e). It was observed that the adherence of the deposited layers was optimal if the wafer was tilted during the O_2 plasma etching and during the deposition of electrodes. So the electrode deposition was done in two steps, one per side of the ridges.

Finally, an innovative lift-off was achieved by lapping the top of the ridge with the circular precision saw, to eliminate the short circuit between signal and ground electrodes, as seen in Fig. 3(f). More precisely, the blade was lowered to a set point above the substrate surface to cut the resist without touching the ridge top. The lift-off step was ended by chemically removing the remaining photoresist on the top. The resulting electrodes are well defined, as shown in Fig. 4(c).

It is worth noting that the innovative mask-less lift off technique is necessary to avoid cracks or metal tearing at the top of the waveguide. For the sake of comparison, we show in Fig. 4(a) an SEM view of electrodes that were achieved by a standard lift off technique, where no preliminary lapping was done before removing the resist. It is clear from the figure that the lapping step is mandatory to avoid the cracks at the top of the electrodes.

To evaluate the interest of ALD in comparison with a standard deposition technique, we have also fabricated another waveguide in the same conditions, except that the ALD step was replaced with evaporation of silica, and the sample was tilted several times during evaporation to coat the entire side of the ridges. The result is seen in Fig. 4(b). Thereby, we can observe that the top of the electrodes is better defined in the case of ALD coating (Fig. 4(c)), but evaporation can nevertheless be an

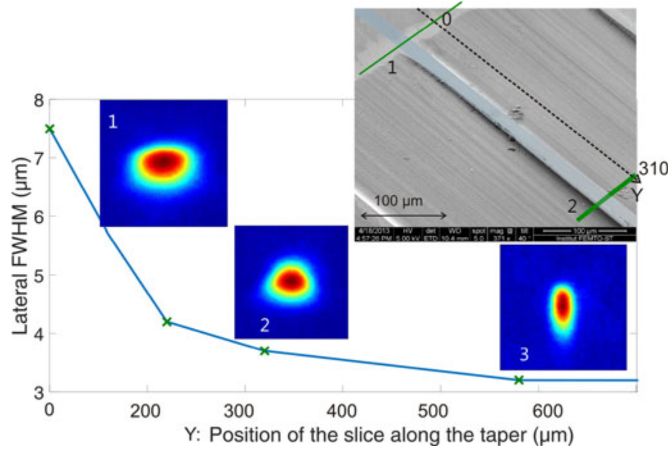

Fig. 5. Experimental results corresponding to a taper with a width of 6 μm. (a) Evolution of the light confinement within the taper as a function of its length for a TE Y-propagating mode. Insert: SEM view of the taper and view of the slices (green lines) that were done to visualize the evolution of the output TE mode. The same tendency was observed for a TM mode.

alternative to ALD if the thickness homogeneity of the dielectric layer is not critical.

B. Characterization of the Tapered-Ridge Waveguides

The tapers were tested by producing several tapered-ridge waveguides as described in the previous section. Then, the extremity of the waveguides was sliced at different lengths as schematically depicted with the green line in the insert of Fig. 5. Each time, light was injected at one extremity of the waveguide, and the spatial distribution of the optical energy was observed at the end of the sliced taper, by means of a 20x objective and a Vidicon camera. The measured results at 1550 nm wavelength are shown in Fig. 5, where the evolution of light confinement in the taper is shown as a function of the position of the slice. The origin Y = 0 corresponds to the extremity of the tapered-ridge, where the height of the ridge is null. As predicted, the output optical mode is tightly laterally confined in the section of the ridge waveguide (point #3 of Fig. 5, Y = 590 μm), where the ridge height is of 20 μm. The lateral confinement weakens progressively with the decrease of the ridge's height. At the output of the taper, the output optical mode corresponds to the one of a standard Ti-indiffused waveguide (point #1 of Fig. 5, Y = 0). These experimental results confirmed the ability of the transition section to act as a Spot-Size Converter.

Then, the optical losses were measured for a 6 μm-wide and 40 μm-high tapered-ridge waveguide. These losses were compared with the ones measured on a 6-μm wide and 40 μm-high Ti-indiffused ridge waveguide done in the same conditions but without any taper, and also with the ones measured on a standard Ti-indiffused waveguide (see Table I).

To assess the global propagation losses $\alpha_{\mathrm{dB/cm}}$ in dB/cm, we measured IL_{min}, $IL_{\max}$, RL_{min}, and $RL_{\max}$, which are respectively the minimum and maximum insertion losses, and the minimum and maximum return losses, all being expressed in fraction [4]. The propagation losses were deduced from the total waveguide length L as described in [4]:

$$\alpha_{\mathrm{dB/cm}} = \frac{10}{L} \cdot \log\left(\frac{\sqrt{RL_{\max} \cdot IL_{\max}} - \sqrt{RL_{\min} \cdot IL_{\min}}}{\sqrt{RL_{\max} \cdot IL_{\max}} + \sqrt{RL_{\min} \cdot IL_{\min}}}\right) \quad (4)$$

They were hence measured to be of $\alpha_{\mathrm{TE}} = 0.12 \pm 0.05$ dB/cm and $\alpha_{\mathrm{TM}} = 0.75 \pm 0.05$ dB/ cm (see third column of Table I). These values were measured to be unchanged after the removal of the tapered section of the waveguide. So the tapers do not induce enhanced propagation losses inside the waveguides, which proves an adiabatic mode conversion between the fiber and the waveguide.

Then, the total insertion losses were measured from a fiber-fiber test coupling. After a reference measurement, the tapered-ridge waveguide was introduced between two cleaved SMF-28 fibers. Light-coupling was achieved at the input and output facets by using a matching index liquid. The total insertion losses were measured to be of $\alpha_{\mathrm{TE}} = 2.4 \pm 0.2$ dB and $\alpha_{\mathrm{TM}} = 3.0 \pm 0.2$ dB at 1.55 μm wavelength for TE and TM polarizations respectively. The transition losses (including transmission losses, coupling losses and radiation losses in the transition) are deduced by subtracting the propagation losses in the 10.0 mm long ridge-section of the tapered-ridge waveguide: they are estimated to be of 1.0 $\pm$ 0.1 dB per transition for both TE and TM polarization. This can be advantageously compared with the measurements performed through the same ridge waveguide without any taper: the measured insertion losses were respectively of $\alpha_{TE} = 5.4 \pm 0.4$ dB and $\alpha_{TM} = 6.1 \pm 0.4$ dB, meaning that the losses are of 2.6 $\pm$ 0.2 dB per facet if there is no taper between the SMF fiber and the ridge. It can thus be concluded that the taper enables a reduction of the losses of 1.6 dB per facet in comparison with a direct fiber-ridge connection, and consequently the total insertion losses are improved by 3.2 dB in presence of the taper at the extremities of the ridge. This 3.2 dB reduction of the insertion losses is attributed to a better mode-matching between the SMF28 fiber and the input of the tapered-ridge waveguide, as compared with a direct

TABLE I
ESTIMATION OF THE LOSSES OF TE AND TM MODES OF Y-PROPAGATING X-CUT TI INDIFFUSED WAVEGUIDES

Waveguide	Pol.	Prop. Losses (dB/cm)	Trans. Loss per facet (dB)	IL (dB)
Standard Ti-indiffused	TE	0.12 ± 0.05	1.0 ± 0.1	2.3 ± 0.2
	TM	0.75 ± 0.05	0.9 ± 0.1	2.5 ± 0.2
Ridge wg	TE	0.15 ± 0.05	2.6 ± 0.2	5.4 ± 0.4
	TM	0.80 ± 0.05	2.7 ± 0.2	6.1 ± 0.4
Tapered-ridge wg	TE	0.13 ± 0.05	1.0 ± 0.1	2.4 ± 0.2
	TM	0.80 ± 0.05	1.1 ± 0.1	3.0 ± 0.2

Comparison between standard waveguides (row 1), single ridge waveguides (row 2) and tapered-ridge waveguides (row 3). The ridges are 6 μm wide and 40 μm high. The taper's length was of 700 μm, and the total length of the tapered ridge waveguide and standard waveguide was of 10 mm. Pol. denotes the polarization state, Prop. Losses corresponds to the global propagation losses, Trans. Loss per facet is the total transition loss at the input and ouptput (including thre Fresnel losses, scattering losses, and coupling losses at the inteface fiber-guide), and IL is the total insertion loss of the waveguide.

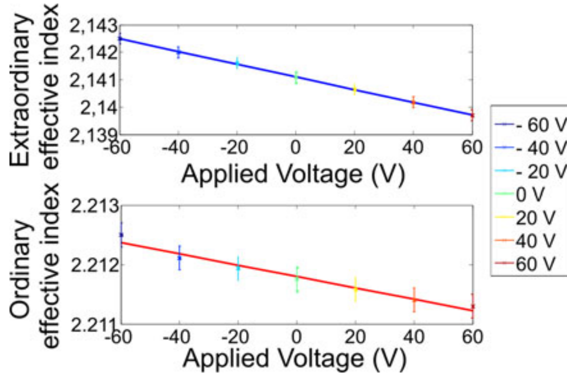

Fig. 6. Assessment of the extraordinary and ordinary refractive index as a function of the applied voltage. The results are extracted from the Free Spectral Range of the transmitted spectra (4).

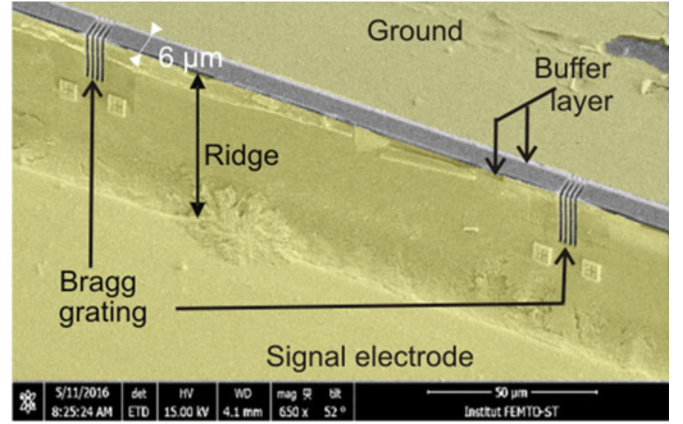

Fig. 7. SEM view of the Fabry-Perot cavity made of two Bragg gratings.

fiber-to-ridge connection, which corroborates the measurement in [9]. Hence, the deposition of the buffer layer and electrodes do not induce optical perturbation of the tapered-ridges.

C. Electro-Optical Characterization of the Ridge Waveguide

The electro-optical efficiency was evaluated by using probes connected to the ground and signal electrodes of the ridge waveguide. The transmitted spectrum through the ridge was measured using a BOSA 100 high resolution optical spectrum analyzer, as a function of applied voltage. As described in [15] Fabry-Perot oscillations appeared in the transmitted spectrum, due to back reflection at the extremities of the waveguide when no liquid index was used. The group effective refractive index *n* was deduced from the Free Spectral Range *FSR* of the oscillations and from the length *L* of the ridge through (5):

$$n = \frac{\lambda^2}{2 \cdot FSR \cdot L} \tag{5}$$

The variation of the refractive index as a function of applied voltage is shown in Fig. 6 for both TE and TM guiding waves.

The group effective refractive index variations are $\Delta n_{\mathrm{TE}}/\Delta V = 2.3{\cdot}10^{-5} \pm 0.2{\cdot}10^{-5}$ RIU/V and $\Delta n_{\mathrm{TM}}/\Delta V = 1.0{\cdot}10^{-5} \pm 0.2{\cdot}10^{-5}$ RIU/V, respectively for the TE and TM guided waves. These results are in good agreement with the theoretical predictions $(\Delta n_{TE}/\Delta V)_{\mathrm{theo}} = 2.2{\cdot}10^{-5}$ RIU/V and $(\Delta n_{TM}/\Delta V)_{\mathrm{theo}} = 0.9{\cdot}10^{-5}$ RIU/V that are calculated from (6) and (7):

$$(\Delta n_{\mathrm{TE}}/\Delta V)_{\mathrm{theo}} = \frac{n_e^3 \cdot r_{33} \cdot \eta}{2 \cdot g} \tag{6}$$

$$(\Delta n_{\mathrm{TM}}/\Delta V)_{\mathrm{theo}} = \frac{n_o^3 \cdot r_{13} \cdot \eta}{2 \cdot g} \tag{7}$$

where $n_{\mathrm{e}} = 2.138$ and $n_{\mathrm{o}} = 2.210$ denote the extraordinary and ordinary refractive index at 1550 nm wavelength respectively, and $r_{33} = 30.8$ pm/V, $r_{13} = 10.1$ pm/V are the $LiNbO_3$ electro-optical coefficients for the TE and TM wave.

These results confirm the very high value of the electro-optical coefficient $\eta = 90\%$, which is two times higher than the EO coefficient of a standard EO waveguide.

Further enhancement of the electro-optical effect can be obtained by writing photonic structures along the optical path.

IV. Ultra-Compact High-Aspect-Ratio EO Modulator

The tapered-ridge waveguide was finally transformed into an intensity modulator by etching two Bragg gratings along the side of the ridge. This step was achieved by focused ion beam (FIB) milling. The Bragg gratings had 4 air grooves, a period of 1.58 μm and a depth of 15 μm. An overview of the microcavity is seen in the SEM picture of Fig. 7. Noteworthy, the very high aspect ratio of the gratings is due to the inscription of the microstructures along the flank of the ridge waveguide rather than on the top [20].

The quality factor of the cavity was measured to be $Q = 2400$, which is far lower than expected from numerical simulations. This weak quality factor is attributed to gallium pollution caused during the FIB milling process. Nevertheless, the electro-optical response of both TE and TM polarization was measured in reflection by applying a probe on the electrodes and by measuring the reflected signal with a fibered circulator connected to a photodetector. The figures of modulation are shown in Fig. 8: the TE and TM guided waves exhibit respectively a half-wave voltage of $V_\pi \mathrm{TE} = 30.5$ V and $V_\pi \mathrm{TM} = 60.5$ V.

Consequently, the measured figures of merit of the Fabry-Perot-based modulator are respectively $V_\pi \mathrm{TE} \cdot L = 0.46$ V·cm and $V_\pi \mathrm{TM} \cdot L = 0.91$ V·cm, which is far lower than the figures of merit of standard Ti-indiffused modulators deduced from (8) and (9):

$$(V_\pi \mathrm{TE} \cdot L)_{\mathrm{std}} = \frac{\lambda \cdot g}{2 \cdot n_e^3 \cdot r_{33} \cdot \eta_{\mathrm{std}}} \tag{8}$$

$$(V_\pi \mathrm{TM} \cdot L)_{\mathrm{std}} = \frac{\lambda \cdot g}{2 \cdot n_o^3 \cdot r_{13} \cdot \eta_{\mathrm{std}}} \tag{9}$$

where $\eta_{\mathrm{std}} = 40\%$ denotes the electro-optical overlap coefficient of a standard waveguide fabricated in the same conditions as the ridge waveguide, but without dicing step. Thereby, we calculate $(V_\pi \mathrm{TM} \cdot L)_{\mathrm{std}} = 3.67$ V·cm and $(V_\pi \mathrm{TM} \cdot L)_{\mathrm{std}} = 10.5$ V·cm. As a consequence, the presented microcavity-based electro-optical modulator shows 8 times and 11 times

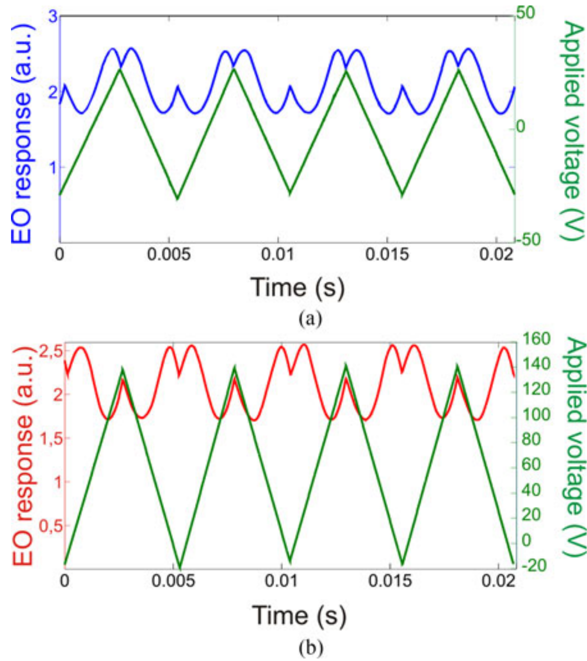

Fig. 8. Electro-optical response of the microcavity-based X-cut modulator propagation in the Y-crystalline direction. (a) TE guided wave. (b) TM guided wave.

enhancement of the EO interaction for the respective TE and TM waves respectively, as compared to standard configuration. This enhancement is even more than 4 times higher than what was reported in the previous paragraph for a single ridge waveguide, and therefore it cannot be attributed solely to the ridge configuration. The enhanced EO sensitivity is rather attributed to a tip effect that increases the electric field in the vicinity of the Bragg grating. As seen in Fig. 7, the Bragg gratings were inscribed inside the electrodes, which act locally as metal pins, and provoke a local enhancement of the applied electric field. Even higher sensitivity is expected by optimizing the optical behavior of the Fabry-Perot cavity.

V. Conclusion

In conclusion, we have developed high-aspect ratio lithium niobate electro-optical ridge waveguides with conformal dielectric buffer layer and vertical electrodes. Precise dicing is used for the production of high ridges, and atomic layer deposition is employed to uniformly coat the ridge sides with a buffer layer. The electrodes are finally deposited on the flanks of the ridge by combining sputtering and an innovative maskless lift-off technique. We have shown that this configuration allows a uniform distribution of the applied electric field. Therefore, the electro-optical overlap coefficient can be expressed simply as a function of the buffer layer thickness and the ridge width. The ridges are made with integrated tapers allowing total insertions losses lower than 3 dB for both TE and TM polarizations. The configuration was used to host a Fabry-Perot-based microcavity made of two high-aspect-ratio Bragg gratings, with a figure of merit of 0.46 V·cm, which is 8 times lower than the one of a standard waveguide. Many other applications such as $LiNbO_3$ MOEMs or EO nonlinear functionalities can now be envisioned thanks to these developments.

References

[1] G. Bettella *et al.*, "Lithium niobate micromachining for the fabrication of microfluidic droplet generators," *Micromachines*, vol. 8, no. 6, pp. 185–198, 2017.

[2] T. Guenther, Z. X. Jiang, K. Kim, and D. D. Sieloff, "Mesa sample preparation for secondary ion mass spectrometry depth profiling using an automated dicing saw," *J. Vac. Sci. Technol. B*, vol. 27, no. 2, pp. 677–680, Jan. 2009.

[3] F. Henrot, F. Bassignot, C. Guyot, J. Y. Rauch, B. Guichardaz, and S. Ballandras, "Highly coupled resonator based on periodically poled lithium niobate ridge," *IEEE Trans. Ultrason., Ferroelect., Freq. Control*, vol. 60, no. 8, pp. 1556–1563, Aug. 2013.

[4] N. Courjal *et al.*, "Simple production of membrane-based $LiNbO_3$ micro-modulators with integrated tapers," *Opt. Lett.*, vol. 41, no. 21, pp. 5110–5113, Nov. 2016.

[5] S. B. Goncalves, M. J. Oliveira, A. C. Peixoto, A. F. Silva, and J. H. Correia, "Out-of-plane neural microelectrode arrays fabrication using conventional blade dicing," *Int. J. Adv. Manuf. Technol.*, vol. 85, pp. 431–442, Oct. 2015.

[6] R. Bhandari, S. Negi, L. Rieth, and F. Solzbacher, "A wafer-scale etching technique for high aspect ratio implantable MEMS structures," *Sensors Actuators A Phys.*, vol. 162, no. 1, pp. 130–136, Jul. 2010.

[7] M. F. Volk, S. Suntsov, C. E. Rüter, and D. F. Kip, "Low loss ridge waveguides in lithium niobate thin films by optical grade diamond blade dicing," *Opt. Express*, vol. 24, no. 2, pp. 1386–1391, Jan. 2016.

[8] L. Ai, L. Wang, Y. Tan, S. Akhmadaliev, S. Zhou, and F. Chen, "Efficient second(harmonic generation of diced ridge waveguides based on carbon ion-irradiated periodically poled LiNbO3," *J. Lightw. Technol.*, vol. 35, no. 12, pp. 2476–2480, Jun. 2017.

[9] N. Courjal *et al.*, "Low-loss $LiNbO_3$ tapered-ridge waveguides made by optical-grade dicing," *Opt. Lett.*, vol. 23, no. 11, pp. 13983–13990, May 2015.

[10] Y. Cheng, S. Akhmadaliev, S. Zhou, and F. Chen, "Optical ridge waveguides in Nd: LGS crystal produced by combination of swift C 5+ ion irradiation and precise diamond blade dicing," *Opt. Laser Technol.*, vol. 81, pp. 122–126, Jul. 2016.

[11] Q. Luan *et al.*, "Optical ridge waveguides in Nd:CNGG disorder laser crystal produced by combination of carbon ion irradiation and precise diamond blade dicing," *Opt. Mater.*, vol. 39, pp. 247–250, Jan. 2015.

[12] M. Chauvet *et al.*, "High efficiency frequency doubling in fully diced $LiNbO_3$ ridge waveguide on silicon," *J. Opt.*, vol. 18, no. 8, Jul. 2016, Art. no. 085503.

[13] S. Suntsov, C. E. Rüter, and D. Kip, "Er: Ti: LiNbO3 ridge waveguide optical amplifiers by optical grade dicing and three-side Er and Ti in-diffusion," *Appl. Phys. B*, vol. 123 no. 4, pp. 118–122, Apr. 2017.

[14] H. Lu *et al.*, "Integrated temperature sensor based on an enhanced pyroelectric photonic crystal," *Opt. Express*, vol. 21, no. 14, pp. 16311–16318, Jul. 2013.

[15] N. Courjal *et al.*, "High aspect ratio lithium niobate ridge waveguides fabricated by optical grade dicing," *J. Phys. D*, vol. 44, no. 30, Jul. 2011, Art. no. 305101.

[16] R. W. Johnson, A. Hultqvist, and F. Bent, "A brief review of atomic layer deposition: from fundamentals to applications," *Mater. Today*, vol. 17, no. 5, pp. 236–246, Jun. 2014.

[17] M. Häyrinen, M. Roussey, A. Säynätjoki, M. Kuittinen, and S. Honkanen, "Titanium dioxide slot waveguides for visible wavelengths," *Appl. Opt.*, vol. 54, no. 10, pp. 2653–2657, Mar. 2015.

[18] M. Häyrinen *et al.*, "Low-Loss Titanium dioxide strip waveguides fabricated by atomic layer deposition," *J. Lightw. Technol.*, vol. 32, no. 2, pp. 208–212, Jan. 2014.

[19] A. Autere *et al.*, "Slot waveguide ring resonators coated by an atomic layer deposited organic/inorganic nanolaminate," *Opt. Express*, vol. 23, no. 21, pp. 26940–26951, Oct. 2015.

[20] C. Guyot *et al.*, "Optical characterization of ultra-short Bragg grating on lithium niobate ridge waveguide," *Opt. Lett.*, vol. 39, no. 2, pp. 371–374, 2014.

Authors' biographies not available at the time of publication.